



Free energy difference to create the M-OH^{*} intermediate of the oxygen evolution reaction by time-resolved optical spectroscopy

Ilya Vinogradov¹, Suryansh Singh^{1,2}, Hanna Lyle^{1,2}, Michael Paolino^{1,3}, Aritra Mandal¹✉, Jan Rossmeisl⁴ and Tanja Cuk^{1,2,5}✉

Theoretical descriptors differentiate the catalytic activity of materials for the oxygen evolution reaction by the strength of oxygen binding in the reactive intermediate created upon electron transfer. Recently, time-resolved spectroscopy of a photo-electrochemically driven oxygen evolution reaction followed the vibrational and optical spectra of this intermediate, denoted M-OH^{*}. However, these inherently kinetic experiments have not been connected to the relevant thermodynamic quantities. Here we discover that picosecond optical spectra of the Ti-OH^{*} population on lightly doped SrTiO₃ are ordered by the surface hydroxylation. A Langmuir isotherm as a function of pH extracts an effective equilibrium constant relatable to the free energy difference of the first oxygen evolution reaction step. Thus, time-resolved spectroscopy of the catalytic surface reveals both kinetic and energetic information of elementary reaction steps, which provides a critical new connection between theory and experiment by which to tailor the pathway of water oxidation and other surface reactions.

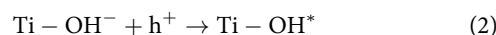
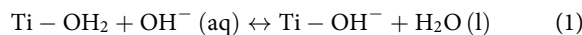
Catalytic reactions are described by a set of meta-stable intermediate chemical forms that reorganize reactants into products¹. Yet, the activity of material surfaces for catalysis has been differentiated largely by their cumulative product evolution, with a primary example being the steady-state current in electrochemical measurements². Given several underlying and separate reaction steps, multiple mechanistic models could explain the same outcome^{3–5}. Thus, there exists a need for experiments to access the individual reaction steps^{4,5}. To do so through the free energy differences (ΔG) between intermediates would directly underpin the theory⁶ and would provide thermodynamic quantities by which to tailor the material and its environment for desired functionality⁷.

One of the most important and studied reactions in this context is the electrochemically driven oxygen evolution reaction (OER) on transition-metal oxide surfaces^{8,9}. The M-OH^{*} intermediate, created upon the first electron and proton transfer from water, is expected to initiate the formation of the first chemical bond of O₂ (O–O), with corresponding free energy differences $\Delta G_1(\text{OH}^*)$ and $\Delta G_3(\text{O–O})$ (refs. ^{6,10}). With scaling relationships¹¹, $\Delta G_1(\text{OH}^*)$ becomes a predictive theoretical descriptor of OER activity: when $\Delta G_1(\text{OH}^*)$ is large, forming M-OH^{*} is rate limiting, and when it is small, forming the O–O bond is rate limiting. However, to date, these thermodynamic and calculated limitations on O₂ evolution have been compared against experiment using the electrochemical current, which is inherently kinetic.

A series of time-resolved studies of photo-electrochemically driven OERs have isolated the spectral and kinetic signatures of the hole-trapping M-OH^{*} intermediate, including titanium oxylys (Ti-O⁻ terminal and Ti-O⁺-Ti in-plane)^{12,13}, the cobalt oxo (Co=O)¹⁴ and the iron oxo (Fe=O)¹⁵. The M-OH^{*} notation is generic for all these intermediates, with H⁺ either bound to the oxygen site or having

transferred to a nearby one^{16,17}. While vibrational spectroscopies determine these detailed bonding geometries^{18,19}, optical spectroscopy^{12,20} revealed easily trackable electronic levels created in the middle of the semiconducting bandgap that target the total population of M-OH^{*}. Using these mid-gap levels, ultrafast optical studies of SrTiO₃ (STO) followed the picosecond formation of the Ti-OH^{*} population from delocalized valence band (VB) holes¹² and its subsequent, microsecond decay towards the next reaction step²¹.

While such time-resolved studies structurally identified transient surface intermediates and provided insight into their role in the catalytic cycle, comparatively little experimental information exists on their energetics. The difficulty lies in finding a methodology that both isolates the reaction steps and captures their thermodynamic properties^{22,23}. In photo-electrochemistry, light excites the reaction instantaneously from a surface prepared by the dark equilibrium with the electrolyte. Therefore, the first proton and electron transfer can be well separated in time, with the proton transfer occurring in the dark and the electron transfer occurring only upon photo-excitation of VB holes:



In reaction (2), h⁺ represents a hole. Using the self-ionization of H₂O into OH⁻ and H⁺, reaction (1) can be written with a product H⁺ instead. Both reactions equivalently describe the acidity of a water-absorbed Ti site. If one adds an electron at the chemical potential of the delocalized hole to each side of reaction (2), the hole-trapping reaction is equivalent to an electron

¹Renewable and Sustainable Energy Institute (RASEI), University of Colorado, Boulder, CO, USA. ²Materials Science and Engineering Program, University of Colorado, Boulder, CO, USA. ³Department of Physics, University of Colorado, Boulder, CO, USA. ⁴Department of Chemistry, University of Copenhagen, Copenhagen, Denmark. ⁵Department of Chemistry, University of Colorado, Boulder, CO, USA.

✉e-mail: aritra.mandal@colorado.edu; tanja.cuk@colorado.edu

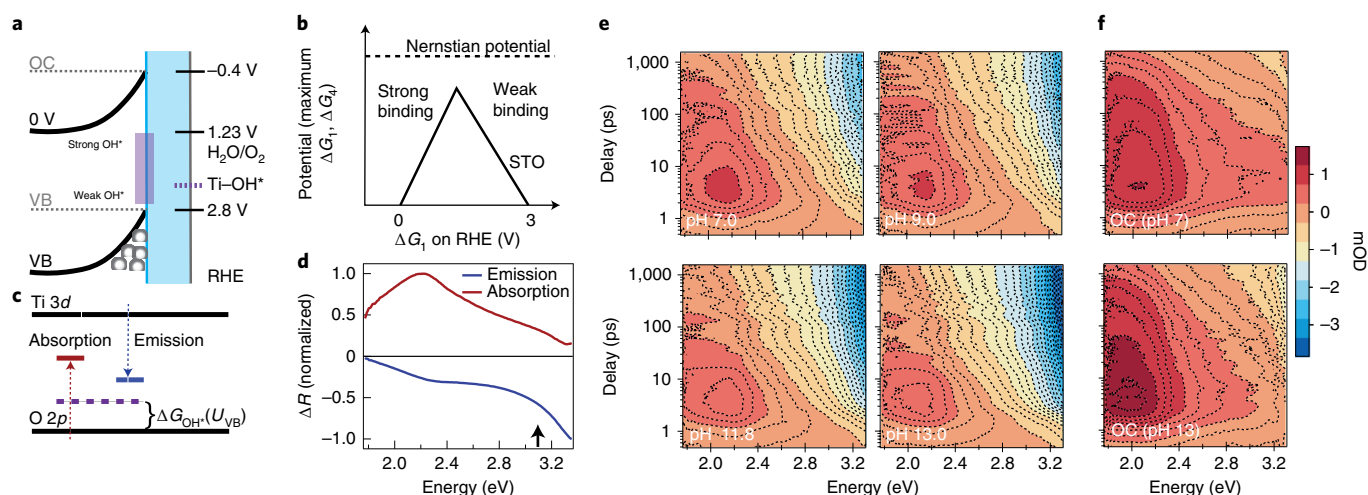


Fig. 1 | Photo-electrochemical configuration and optical spectra. **a**, Cartoon of energy level alignments at closed circuit (0 V versus SCE) and at open circuit (OC) on the RHE scale (pH 0) at the solid–electrolyte (–white-light blue) interface. The purple block indicates the redox level of M–OH[•] intermediates for different oxygen binding strengths. The grey open circles represent VB holes. **b**, Volcano plot of OER theoretical analysis, for which the minimum potential needed to drive the reaction spontaneously is depicted as a function of $\Delta G_1(\text{OH}^\bullet)$; strong and weak oxygen-binding branches are denoted. **c**, Cartoon of the optical transitions induced by Ti–OH[•] intermediates, leading to emission (blue arrow) and absorption (red arrow). The dashed purple level corresponds to the redox level for creating Ti–OH[•], also depicted in **a**. The absorptive and emissive transitions are vertical ones, which involve states in the CB and VB, respectively, that are at the reaction coordinate of the distorted Ti–O bonds in Ti–OH[•]; the difference in the blue and red lines reflects that these are separate potential energy surfaces. **d**, Normalized emission and absorption derived by a constrained, singular value decomposition of the optical spectra in **e**. The black arrow corresponds to the STO bandgap. **e**, Transient optical spectra of the absorption (red) and emission (blue) in the visible regime for select pH at closed circuit. From the raw data, the acoustic phonon oscillations have been removed (Supplementary Fig. 6). The colour scale is the optical density of the measured change in reflectivity (mOD or 10^{-3} OD), positive for absorption and negative for emission. **f**, Transient optical spectra at open circuit (OC) for pH 7 and pH 13 on the same mOD scale as the closed circuit data.

transfer out of the electrode, such that the two reactions net to $\text{Ti-OH}_2 \rightarrow \text{Ti-OH}^\bullet + \text{H}^+ + \text{e}^-$ where e^- represents an electron.

The first reaction is an explicit equilibrium defined by the free energy difference for surface hydroxylation, $\Delta G_{\text{OH}^\bullet}$, or equivalently, the pK_a of Ti–OH₂. The second reaction forms a meta-stable species, where $\Delta G_{\text{OH}^\bullet}(U_{\text{VB}})$ is the free energy difference between a hole at the VB edge potential (U_{VB}) and a trapped hole, Ti–OH[•]. U_{VB} is utilized since the photo-excited holes are presumed to thermalize to the VB edge before transfer given the inefficiency of hot-hole transfer from bulk semiconductor crystals^{24,25}. By being separable, the surface hydroxylation prior to light excitation can shift the reaction equilibria, which allows our work to identify $\Delta G_1(\text{OH}^\bullet)$ by time-resolved optical spectra. In particular, the sigmoidal pH dependence of the picosecond Ti–OH[•] population generates a Langmuir isotherm of a meta-stable intermediate on the photo-driven surface. For surfaces in which the hydroxylation can be modulated in an accessible pH range, the work closes a vital missing gap between the observation of the kinetics and structure of catalytic intermediates and experimental determination of the energetics of elementary steps. The results show how reaction kinetics, inherent in experimental investigations, can begin to be analysed with respect to measured, rather than largely theoretical, free energy differences.

Transient optical spectra of the electrochemical interface

Figure 1 shows the primary pH-dependent optical spectra from which we draw our conclusions. The transient data are taken under steady-state conditions of photo-electrochemical O₂ evolution using pulsed (150 fs, 500 Hz) bandgap (266 nm, 4.66 eV) excitation of n-doped STO (n-STO; 0.1%, 0.5% and 0.7% Nb STO) described previously and in detail in Supplementary Figs. 1–3. Here, the surface is probed by a broad-band optical pulse (375–700 nm, 1.7–3.3 eV). While there is a high quantum efficiency of charge separation ($\sim 75\%$), side reactions do affect the sample surface. Therefore, to obtain the high-quality kinetic

data, we employ a continuous scanning method (Supplementary Fig. 4). At a photo-excitation density of 0.04 mJ cm^{-2} , one maintains a constant steady-state current to within 0.5% in a single measurement (Supplementary Fig. 3), which corresponds to a turnover frequency of $\sim 1 \text{ O}_2$ per site per second of the illuminated area. The cartoon (Fig. 1a) shows the level alignment of the valence and conduction bands of STO with the Nernstian potential of water oxidation on the reversible hydrogen electrode (RHE) scale. The primary data are taken with a constant 0 V versus saturated calomel electrode (SCE) applied to the back of the electrode. A constant 0 V versus SCE is chosen to maintain the same potential drop across the part of the electric double layer that involves free ions in the electrolyte (phosphate, sulfate, OH[−], H⁺), such that reaction (1) can be considered fairly independently of salt concentration (Supplementary Fig. 2). With this electrochemical configuration, the Schottky barrier will necessarily increase with pH due to the interfacial Ti–OH[−] dipole²⁶ (Supplementary Figs. 1 and 2). Data taken at open circuit aid in the assignment of spectral components and in the interpretation of the pH dependence. Finally, 0.1% Nb and 0.7% Nb STO were characterized for hydroxylation at near neutral conditions by ambient pressure X-ray photoelectron spectroscopy (Supplementary Fig. 5).

Upon excitation, a delocalized hole in the valence band can relax to create Ti–OH[•]. When a hole traps to an oxygen site, the Ti–O distances distort and mid-gap levels form, as described in detail for TiO₂ (refs. 16,17) and for STO (refs. 12,27,28). These mid-gap levels are relateable to $\Delta G_1(\text{OH}^\bullet)$ by the $\Delta G_{\text{OH}^\bullet}(U_{\text{VB}})$ of reaction (2):

$$\Delta G_1(\text{OH}^\bullet) = \text{VB} + \Delta G_{\text{OH}^\bullet}(U_{\text{VB}}) \quad (3)$$

The redox level (RHE) corresponding to $\Delta G_1(\text{OH}^\bullet)$ for STO is shown schematically in Fig. 1a (purple dotted line). The pH dependence of reaction (1) is that of the RHE scale ($-59 \text{ mV per pH unit}$), which results from a cathodically increasing VB edge

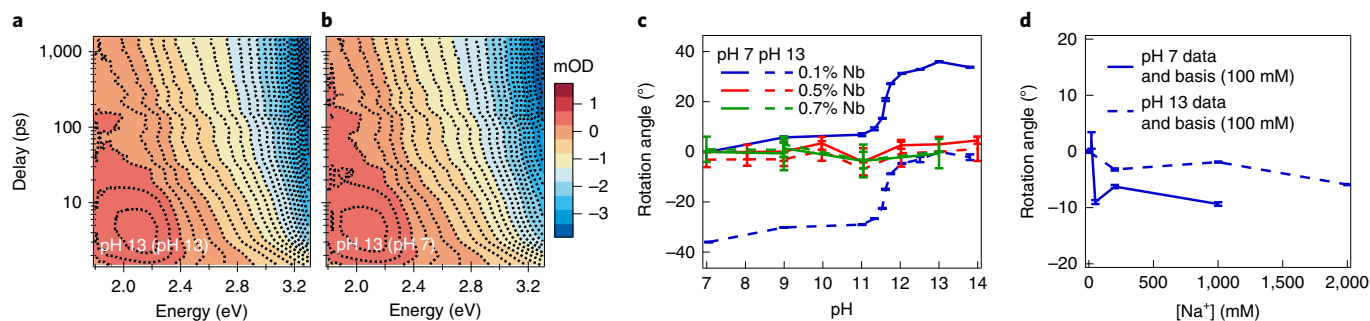


Fig. 2 | SVD and rotation analysis. **a**, Reconstruction of the pH 13 spectrum from its first two SVD components. **b**, Reconstruction of the spectrum in **a** from the spectral SVD components of the pH 7 transient optical spectra. **c**, Rotation angle analysis for the phosphate-buffered pH dataset showing a sigmoidal trend across pH in 0.1% Nb STO. The angle is given relative to the pH 7 data in solid lines and relative to the pH 13 dataset in dotted lines. Data are shown for all three STO samples (0.1%, 0.5% and 0.7% Nb). **d**, Rotation angle analysis for the dataset showing little trend with salt concentration for pH 7 (red) and pH 13 (blue) in a $\text{Na}_2\text{SO}_4/\text{NaOH}$ solution. In both pH 7 and pH 13, the reference spectral components are from the corresponding 100 mM $[\text{Na}^+]$ spectral map. For **c** and **d**, error bars indicate the standard deviation of the four angles in the rotation matrix R , which measures how orthogonal the transformation is between the reference and final spectral components.

due to the interfacial dipole²⁶. With equation (3), $\Delta G_1(\text{OH}^-)$ for different materials can also be placed within the bandgap of STO (purple block, Fig. 1a), rising within the gap and lower on the RHE scale for stronger oxygen binding within $\text{M}-\text{OH}^-$ (volcano plot, Fig. 1b).

Emissive optical transitions in the visible regime (blue arrow, Fig. 1c, blue emission, Fig. 1d) result from conduction band (CB) electrons transitioning to the newly created $\text{Ti}-\text{OH}^-$ at the distorted reaction coordinate (blue line, Fig. 1c). Photoluminescence of STO samples routinely assigns the spontaneous emission peak between 2.4 eV and 2.8 eV to localized holes^{27,29,30}. The recent transient optical spectroscopy during OER characterized the stimulated emissive optical dipole transitions¹² by a 1.3 ps kinetic growth, which also occurred in the vibrational spectroscopy identifying the titanium oxyl ($\text{Ti}-\text{O}^-$)¹³. Here, the broad-band probe records this emission in time for lightly doped Nb 0.1% STO as a function of pH (Fig. 1e). From these optical spectra, acoustic phonon oscillations have been subtracted out (Supplementary Fig. 6). The emission (blue) appears clearly during in situ OER and increases with higher pH (Fig. 1e and Supplementary Fig. 7) but is independent of salt concentration (Supplementary Fig. 8); at open circuit conditions for which electrons can more easily recombine with $\text{Ti}-\text{OH}^-$, the emission is much less pronounced but has the same trend with pH (Fig. 1f and Supplementary Fig. 7) and salt (Supplementary Fig. 8). Moreover, the emission appears dominantly as a ~ 2 ps kinetic growth after the initial excitation, as expected for an exoergic $\Delta G_{\text{OH}^-}(\text{V}_{\text{VB}})$, with the timescale assigned previously¹².

Alongside this emissive transition, an absorptive transition (red arrow, Fig. 1c, red absorption, Fig. 1d) also exists. We find the absorption to be less sensitive to the $\text{Ti}-\text{OH}^-$ population: the absorption appears most prominently at open circuit, exhibits decay kinetics and is not substantially modulated by surface conditions (pH). An absorptive transition in the visible regime could arise from VB electrons promoted to an excited potential energy surface (red line, Fig. 1c) for which the $\text{Ti}-\text{O}$ distortion is maintained and a VB hole is left behind, as proposed for titania¹⁶ and other transition-metal oxides^{31,32}. A red-shifted absorption to the emission has been attributed to the intermediate population in iron oxide²⁰ but to the VB hole population in a variety of oxides^{33–35}. Since the proposed absorptive transition is modulated by the VB density of states for hole occupation, a function of both trapped and VB holes, one might expect the kinetics to exhibit a complex interplay of the two populations. By contrast, the CB electron density of states responsible for the emissive transition is independent of the trapped hole

population. The anticipated optical transitions are further discussed in Supplementary Fig. 9.

Principal component analysis of the optical spectra

The spectra shown in Fig. 1d are the result of a principal component analysis constrained^{36,37} to have a pure emissive component and an absorptive one. We first show how two predominant spectral components exist in common for the full dataset. Singular value decomposition³⁸ (SVD; Supplementary Fig. 10) directly yields two dominant components for each reaction condition. If these are common to the dataset, one should be able to reconstruct one reaction condition's optical spectra from a linear combination of the principle components of another, or

$$M^{(\text{pH}13)} \approx \left(U_{1,2}^{(\text{pH}7)} \cdot R^{-1} \right) \cdot S_{1,2}^{(\text{pH}13)} \cdot \left(V_{1,2}^{(\text{pH}13)} \right)^T \quad (4)$$

$M^{(\text{pH}13)}$ is a matrix of the spectral-kinetic data at pH 13. The columns of $U_{1,2}^{(\text{pH})}$ and $V_{1,2}^{(\text{pH})}$ are orthonormal and represent the SVD spectra and kinetics, respectively; T denotes transpose. $S_{1,2}^{(\text{pH}13)}$ is a diagonal matrix that defines the singular values of the two components. The linear combination matrix is $R = \left(U_{1,2}^{(\text{pH}13)} \right)^T U_{1,2}^{(\text{pH}7)}$. If a common two-component basis exists, R will be a rotation matrix (accounting for reflections).

We show the similarity between the pH 13 dataset reconstructed from its own two SVD components in Fig. 2a and the pH 7 SVD components in Fig. 2b. The rotation matrix can be calculated for any pair of reaction conditions within a dataset with small error bars. This rotation analysis shows a sigmoidal pH dependence already encoded in the 0.1% Nb STO data by a common basis set without constraints (Fig. 2c) and quantifies little dependence of the spectral components on the salt concentration (Fig. 2d). It also shows little pH dependence for highly doped (0.5%, 0.7% Nb) STO (Fig. 2c).

Modulating the $\text{Ti}-\text{OH}^-$ reaction equilibria by pH

While the above establishes that a clear and quantifiable trend in pH exists, it does not in itself assign a spectral component to the $\text{Ti}-\text{OH}^-$ population and its origin from reaction (2). We start with a cartoon of the hydrated STO surface in the dark and under photo-excitation (Fig. 3a). The undoped STO surface is understood to partially dissociate H_2O at neutral conditions^{39–41}, such that approximately half the titania sites are water absorbed and

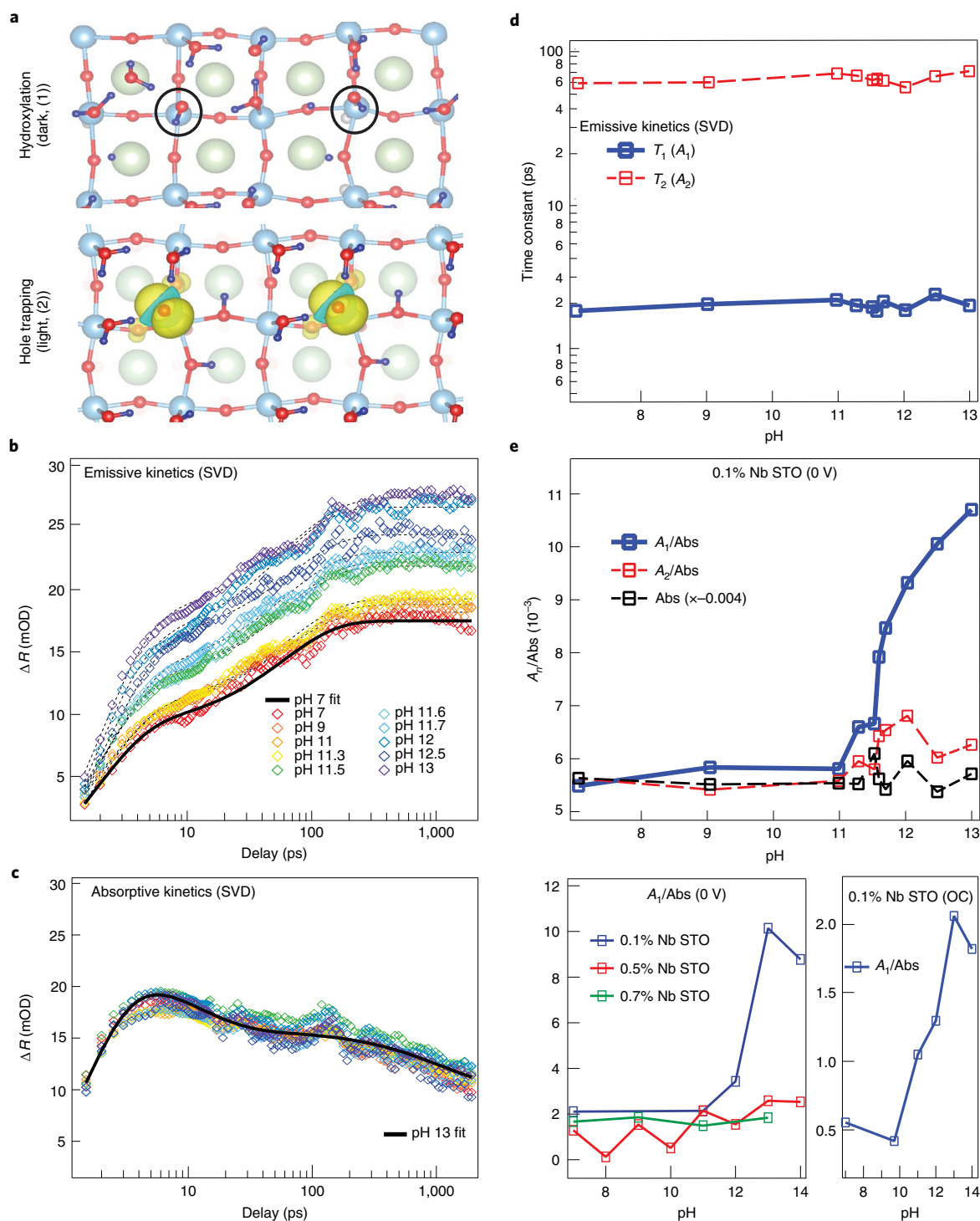


Fig. 3 | Constrained SVD analysis and extraction of 2 ps Ti-OH' population. **a**, Cartoon of the 0.1% Nb STO surface in the dark and upon light excitation, reflecting the two separable proton and electron transfer steps. Red atoms are O, blue atoms are Ti and green atoms are Sr. The Ti-OH⁻ are denoted by black circles, and the orbital of hole trapping on Ti-OH⁻ is yellow. **b**, Weighted, emissive growth kinetics ($X^{-1}S_{1,2}(V_{1,2})^T$)₁ on a mOD scale as a function of pH (coloured diamonds) fit with two rising exponentials (black solid and dotted lines). **c**, The same as **a**, but for the weighted, absorptive decay kinetics ($X^{-1}S_{1,2}(V_{1,2})^T$)₂. **d**, The time constants of the two rising exponentials for the emissive kinetics as a function of pH. **e**, The populations (A_1, A_2) defined by the two time constants, normalized by the integrated absorption (A_i/Abs), as a function of pH; and the integrated absorptive signal (Abs) as a function of pH. Bottom left: A_i/Abs is compared for the three n-STO samples, 0.1%, 0.5% and 0.7% Nb, taken on a new optical set-up (Supplementary Figs. 12–14). These analyses are for data taken at 0 V versus SCE. Bottom right: A_i/Abs is shown for 0.1% Nb STO under OC conditions with sulfate buffer.

half hydroxylated. The lightly doped 0.1% Nb STO surface exhibits a similar ratio of hydroxylation to water absorption by ambient pressure X-ray photoelectron spectroscopy in Supplementary Fig.

5. Since they are separated by Ti-OH₂ groups, the isolated Ti-OH⁻ are well positioned to trap holes quickly (reaction (2)). Further, given the above dichotomy between the emission and absorption,

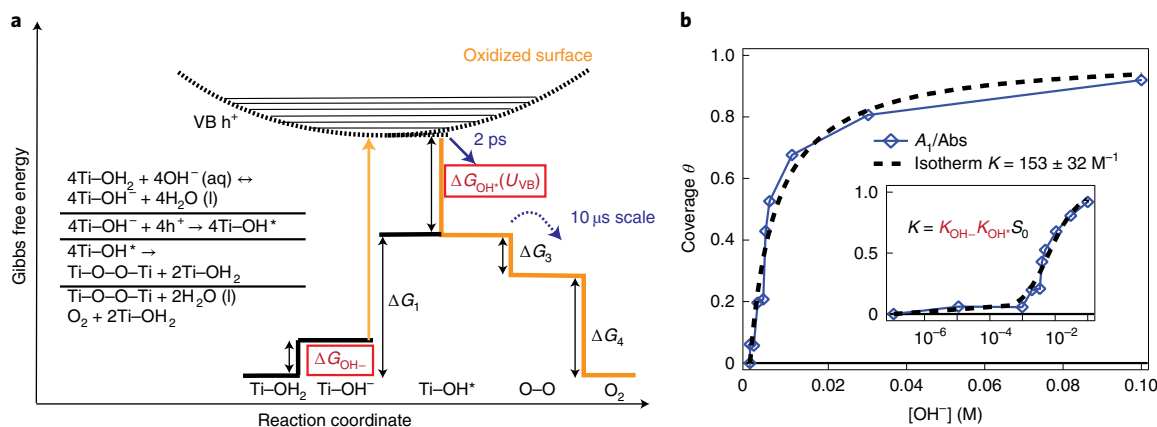


Fig. 4 | Langmuir isotherm model and the effective equilibrium constant (K). **a**, Free energy diagram of Ti-OH⁻ adsorption and Ti-OH['] creation in the context of the full reaction scheme. Photo-excitation (yellow arrow) separates the diagram into the dark, equilibrated and oxidized free energy surfaces. The black dotted line represents the excited hole in the VB, while the yellow solid line represents the pathway to O₂ for a photo-excited hole. The ΔG for each reaction step per site in OER is shown in the standard state, with the ones relevant to the experiment highlighted in red. The time constant (2 ps) for Ti-OH['] creation from the VB hole highlighted in this work is shown by the blue arrow; the dotted blue arrow (on the scale of 10 μ s) denotes the downhill reaction kinetics for O-O bond formation, as suggested by previous work²¹. The full, multi-site reaction scheme suggested by this diagram is stated to the left. **b**, The A_1/Abs component (blue triangles) of 0.1% Nb STO in Fig. 3e at 0 V versus SCE, where the pH 7 contribution has been subtracted and the pH 14 contribution is normalized to 1. The data points have been fit to the Langmuir isotherm described by equations (6) and (7) in the text, with coverage $\theta = [\text{Ti-OH}^*]/h_0^+$ and $K_{\text{eff}} = 153 \pm 32 \text{ M}^{-1}$. The inset shows the agreement on a logarithmic scale with the characteristic sigmoidal behaviour of an isotherm.

a constrained SVD analysis identifies the rising components of the Ti-OH['] population using

$$M \approx (U_{1,2} \cdot X) \cdot (X^{-1} S_{1,2} (V_{1,2})^T) \quad (5)$$

Here, X is a new matrix that describes the projection of the raw SVD components $U_{1,2}$ onto purely emissive (1) and absorptive (2) spectral components. The procedure is outlined in the Supplementary Information (SupplementarySection VI and Supplementary Fig. 11). The emissive spectrum (Fig. 1d) increases with shorter wavelengths, which may be related to the probe stimulating electrons closer to the surface. The absorptive spectrum has a peak near $\sim 2 \text{ eV}$, as identified in a number of other oxides^{16,31,32}.

Figure 3b shows the constrained kinetics associated with emission, $(X^{-1} S_{1,2} (V_{1,2})^T)_1$, for each pH at 0 V versus SCE. While the kinetics exhibit consistent growth rates across pH, the response amplitude systematically increases. However, the kinetics associated with absorption, $(X^{-1} S_{1,2} (V_{1,2})^T)_2$, exhibit decay kinetics and show little change with pH (Fig. 3c). Fitting the emissive curve with two rising exponentials defines the two timescales ($\tau_1 \approx 2 \text{ ps}$ and $\tau_2 \approx 60 \text{ ps}$) shown in Fig. 3d. Since the time-integrated absorption is independent of pH, we can use it to normalize the emission for fluctuations in pump-probe overlap. In Fig. 3e, we show the normalized emissive response as a function of pH and for different experimental conditions. For 0.1% Nb STO, the amplitude of the fast, 2 ps rise (A_1) has a clear sigmoidal dependence on pH centred at 11.7. However, the same analysis of 0.5% and 0.7% Nb STO shows little pH dependence, reflecting the rotation analysis (Fig. 2c); the highly doped STO optical data is shown (Supplementary Fig. 12) and analysed further (Supplementary Figs. 13 and 14) in Supplementary Section VII. For 0.1% Nb STO, the amplitude of the 60 ps rise (A_2) is also fairly pH independent. While in this analysis A_1 and A_2 both report on the Ti-OH['] population, since A_2 occurs later, A_2 represents either a time evolution of the 2 ps Ti-OH['] population or a separate population of Ti-OH['] arising from a different source. While the pH dependence shown in Figs. 1 and 3 is taken

with a phosphate-buffered solution that allows for finer steps in pH, a sigmoidal pH dependence also occurs for A_1 with a sulfate solution (Supplementary Fig. 15). Importantly, the same methodology extracts a sigmoidal pH dependence from the open-circuit data (Fig. 3e and Supplementary Fig. 16) for which no surface degradation exists and photo-excitation flattens the Schottky barrier; this independently isolates the effect as coming from the interfacial hydroxylation.

These results establish a sigmoidal pH dependence for the 2 ps component of Ti-OH['] creation from VB holes, which reflects a reaction isotherm and the two reaction steps proposed above. The fast timescale for the A_1 population aids in separating reaction (1) from (2), since any re-equilibration with OH⁻ in solution should occur at substantially longer timescales^{42,43}. It also suggests that the hole transfer occurs without a simultaneous full proton transfer to solution. This is similarly anticipated by ab initio molecular dynamics simulations on titania^{16,17}. The absence of a clear H/D kinetic isotope effect (Supplementary Fig. 17) substantiates the lack of free H⁺ as a product^{44,45}.

The two separable reactions are also supported by investigating a similar sample, but one for which the surface is expected to be hydroxylated already under neutral conditions. The 0.7% Nb STO indeed exhibits a much higher hydroxylation than 0.1% Nb STO by ambient pressure X-ray photoelectron spectroscopy, with a factor of 2–3 increase at high relative humidity (Supplementary Fig. 5); the more-electron-dense, in-plane, lattice oxygen sites could promote H₂O dissociation⁴⁶. Since the optical spectra for both 0.5% and 0.7% Nb STO also do not exhibit a resolvable pH dependence, the results reflect a dark equilibrium that cannot be pushed by pH in basic conditions. In contrast to the more isolated, defect Ti-OH⁻ sites in lightly doped STO, a fully hydroxylated surface in highly doped STO could reflect a two-dimensional network for hole trapping.

A Langmuir isotherm with an effective equilibrium constant

The free energies of the relevant steps are depicted within the full photo-driven OER reaction in Fig. 4a. Reaction (1) is described by the chemical potential of Ti-OH⁻ relative to Ti-OH₂ along the

same free energy surface in the dark (solid black lines). However, reaction (2) involves a crossing of two distinct surfaces, where the light pulse (yellow arrow) first creates the hole on the oxidized surface at the reaction coordinate defined by the reduced VB but then quickly transfers to the surface for which the trapped hole, Ti-OH^{\cdot} , is a minimum.

We now turn to the description of the sigmoidal pH dependence using a Langmuir-type reaction isotherm, albeit for a meta-stable intermediate population. The model and its application is developed in detail in Supplementary Section X. In a Langmuir isotherm, the sigmoidal rise of the product, an adsorbed surface species, with respect to a tunable reactant concentration reflects the equilibrium constant of the reaction. The saturation in the sigmoid reflects a limiting equation that restricts occupied and unoccupied sites to exchange with each other up to a maximum coverage⁴⁷. For the simple adsorption isotherm of reaction (1), Ti-OH^- exchanges with Ti-OH_2 , the tunable reactant is OH^- and the limiting equation is $S_0 = [\text{Ti-OH}^-] + [\text{Ti-OH}_2]$; S_0 is the total surface site density. However, reaction (2) involves an exchange between delocalized and trapped holes and is tuned by the surface hydroxylation, Ti-OH^- . The limiting equation compatible with a Langmuir isotherm is $h_0^+ = [h^+] + [\text{Ti-OH}^{\cdot}]$; h_0^+ represents the total hole density excited by a single laser pulse, which is kept constant at 2% of the surface site density. In this model, Ti-OH^- independently modulates the isotherm for Ti-OH^- coverage, since Ti-OH^- does not re-equilibrate with OH^- on the picosecond timescale. Therefore, the isotherm of reaction (2) can be written in terms of $[\text{OH}^-]$ by using $[\text{Ti-OH}^-]$ established in the dark, leading to the following net isotherm for the coverage θ :

$$\theta = \frac{[\text{Ti-OH}^{\cdot}]}{h_0^+} = \frac{K_{\text{eff}} [\text{OH}^-]}{1 + K_{\text{eff}} [\text{OH}^-]} \quad (6)$$

$$K_{\text{eff}} = K_{\text{OH}^-} - K_{\text{OH}^+} S_0 \quad (7)$$

Here, K_{eff} is the effective equilibrium constant of both reactions, where $K_{\text{OH}^-} = [\text{Ti-OH}^-]/[\text{Ti-OH}_2][\text{OH}^-]$ and $K_{\text{OH}^+} = [\text{M-OH}^{\cdot}]/[\text{M-OH}^-][h^+]$. The $[\text{OH}^-]$ is in units of M^{-1} , while the rest of the reactants ($[\text{Ti-OH}^-]$, $[\text{Ti-OH}_2]$, $[h^+]$) carry areal number density (for example, cm^{-2}). Therefore, K_{eff} carries a total unit of M^{-1} . The sigmoidal dependence of the extracted coverage is well described by an isotherm with a fitting constant of $K_{\text{eff}} = 153 \pm 32 \text{ M}^{-1}$ reflecting the $\text{pH} = 11.7$ half-rise. A K_{eff} within this error was obtained also for data through $\text{pH} 14$ (Supplementary Fig. 18); that the isotherm saturates is also apparent in the rotation analysis (Fig. 2c). It is important to note that this K_{eff} is in the context of a continually downhill catalytic cycle for which a meta-stable population is being isolated, rather than a reaction that reaches completion.

We now estimate the anticipated value of K_{eff} from theoretical calculations. In theoretical calculations, each VB hole is tied to a Ti-OH^- surface site and does not appear as a separate concentration¹⁶. Therefore, obtaining a theoretical equilibrium constant, K_{eff} , requires dividing K_{eff} by $[h_0^+]$, which represents the degeneracy of the VB hole states upon photo-excitation. With a $\text{p}K_a$ of the Ti-OH_2 site of 8 (ref. 48) and $\Delta G_{\text{OH}^{\cdot}}(U_{\text{VB}}) = -0.4 \text{ eV}$ (refs. 12,27), the derived measured value ($K_{\text{eff}} \approx 5 \text{ M}^{-1}$ with a half-rise near $\text{pH} 13$) comes within a factor of ~ 20 of the observed $K_{\text{eff}} \approx 150 \text{ M}^{-1}$. However, this is approximate since calculated $\Delta G_{\text{OH}^{\cdot}}(U_{\text{VB}})$ values vary and not all holes need to arrive as Ti-OH^{\cdot} through hydroxylated sites modulated by pH in basic conditions. We leave this quantification for future work.

We now obtain the electrochemically driven redox level for the first proton and electron transfer of OER. Using equation (3), with a calculated $\Delta G_{\text{OH}^{\cdot}}(U_{\text{VB}}) = -0.4 \text{ eV}$ consistent with the isotherm and a 2.8 V VB versus RHE for STO (ref. 26), $\Delta G_1(\text{OH}^{\cdot}) = 2.4 \text{ V}$ versus

RHE in the standard state, which places STO comfortably on the weak-binding branch of the usual volcano plots (Fig. 1b)^{10,11}. In applying equation (3), $\Delta G_{\text{OH}^{\cdot}}(U_{\text{VB}})$ is a constant across the pH range. Further insight into the weak binding derives from how much $\Delta G_{\text{OH}^{\cdot}}(U_{\text{VB}})$ leads to a sigmoidal half-rise close to the $\text{p}K_a$ of Ti-OH_2 ; it occurs at $\text{pH} 11.7$ rather than at 8 (ref. 48). An increasingly more exoergic $\Delta G_{\text{OH}^{\cdot}}(U_{\text{VB}})$ would be needed to move the half-rise towards 8. The weak binding and the downhill pathway towards O–O bond formation observed previously²¹ support the full multi-site reaction mechanism of Fig. 4a, where the first electron transfer creates four Ti-OH^{\cdot} intermediates from four H_2O molecules, and then subsequent thermo-chemical reaction steps form O_2 and release two H_2O molecules.

Conclusions

This work discovers a methodology for obtaining equilibrium constants of meta-stable surface intermediates of a driven catalytic reaction using Langmuir isotherms and time-resolved optical spectra of the intermediate population. In particular, we constructed an effective equilibrium constant that defines the reactive Ti-OH^{\cdot} population during water oxidation to O_2 . It is in the range of 10^2 due primarily to the combination of an endoergic ΔG_{OH^-} for surface hydroxylation and an exoergic $\Delta G_{\text{OH}^{\cdot}}(U_{\text{VB}})$ for VB hole trapping. In this regard, the work finds experimental evidence to categorize STO as an electro-catalyst whose energy efficiency is limited by creating rather than removing bound Ti-OH^{\cdot} intermediates, as predicted by theoretical calculations. More generally, the results demonstrate how time-resolved spectroscopic investigations of the water oxidation reaction can reveal the free energy differences of elementary reaction steps, uniquely establishing a necessary connection between thermodynamic and kinetic quantities that guide theory and experiment, respectively.

Online content

Any methods, additional references, Nature Research reporting summaries, source data, extended data, supplementary information, acknowledgements, peer review information; details of author contributions and competing interests; and statements of data and code availability are available at <https://doi.org/10.1038/s41563-021-01118-9>.

Received: 10 September 2020; Accepted: 24 August 2021;
Published online: 1 November 2021

References

- Hammer, B. & Norskov, J. K. Theoretical surface science and catalysis—calculations and concepts. *Adv. Catal.* **45**, 71–129 (2004).
- Markovic, N. M. Electrocatalysis: interfacing electrochemistry. *Nat. Mater.* **12**, 101–102 (2013).
- Seh, Z. W. et al. Combining theory and experiment in electrocatalysis: insights into materials design. *Science* **355**, eaad4998 (2017).
- Weckhuysen, B. M. Chemical imaging of spatial heterogeneities in catalytic solids at different length and time scales. *Angew. Chem. Int. Ed.* **48**, 4910–4943 (2009).
- Buurmans, I. L. C. & Weckhuysen, B. M. Heterogeneities of individual catalyst particles in space and time as monitored by spectroscopy. *Nat. Chem.* **4**, 873–886 (2012).
- Rossmeisl, J., Qu, Z. W., Zhu, H., Kroes, G. J. & Norskov, J. K. Electrolysis of water on oxide surfaces. *J. Electroanal. Chem.* **607**, 83–89 (2007).
- Norskov, J. K. et al. The nature of the active site in heterogeneous metal catalysis. *Chem. Soc. Rev.* **37**, 2163–2171 (2008).
- Zhang, M. & Frei, H. Towards a molecular level understanding of the multi-electron catalysis of water oxidation on metal oxide surfaces. *Catal. Lett.* **145**, 420–435 (2014).
- Kern, J. et al. Structures of the intermediates of Kok's photosynthetic water oxidation clock. *Nature* **563**, 421–425 (2018).
- Man, I. C. et al. Universality in oxygen evolution electrocatalysis on oxide surfaces. *ChemCatChem* **3**, 1159–1165 (2011).
- Busch, M. et al. Beyond the top of the volcano? – A unified approach to electrocatalytic oxygen reduction and oxygen evolution. *Nano Energy* **29**, 126–135 (2016).

12. Chen, X. et al. The formation time of Ti-O• and Ti-O•-Ti radicals at the n-SrTiO₃/aqueous interface during photocatalytic water oxidation. *J. Am. Chem. Soc.* **139**, 1830–1841 (2017).
13. Herlihy, D. M. et al. Detecting the oxyl radical of photocatalytic water oxidation at an n-SrTiO₃/aqueous interface through its subsurface vibration. *Nat. Chem.* **8**, 549–555 (2016).
14. Zhang, M., de Respinis, M. & Frei, H. Time-resolved observations of water oxidation intermediates on a cobalt oxide nanoparticle catalyst. *Nat. Chem.* **6**, 362–367 (2014).
15. Zandi, O. & Hamann, T. W. Determination of photoelectrochemical water oxidation intermediates on hematite electrode surfaces using operando infrared spectroscopy. *Nat. Chem.* **8**, 778–783 (2016).
16. Cheng, J., VandeVondele, J. & Sprik, M. Identifying trapped electronic holes at the aqueous TiO₂ interface. *J. Phys. Chem. C* **118**, 5437–5444 (2014).
17. Chen, J., Li, Y. F., Sit, P. & Selloni, A. Chemical dynamics of the first proton-coupled electron transfer of water oxidation on TiO₂ anatase. *J. Am. Chem. Soc.* **135**, 18774–18777 (2013).
18. Kraack, J. P. & Hamm, P. Surface-sensitive and surface-specific ultrafast two-dimensional vibrational spectroscopy. *Chem. Rev.* **117**, 10623–10664 (2017).
19. Kraack, J. P., Kaeck, A. & Hamm, P. Surface enhancement in ultrafast 2D ATR IR spectroscopy at the metal-liquid interface. *J. Phys. Chem. C* **120**, 3350–3359 (2016).
20. Klahr, B., Gimenez, S., Fabregat-Santiago, F., Bisquert, J. & Hamann, T. W. Photoelectrochemical and impedance spectroscopic investigation of water oxidation with “Co-Pi”-coated hematite electrodes. *J. Am. Chem. Soc.* **134**, 16693–16700 (2012).
21. Chen, X., Aschaffenburg, D. J. & Cuk, T. Selecting between two transition states by which water oxidation intermediates decay on an oxide surface. *Nat. Catal.* **2**, 820–827 (2019).
22. Libuda, J., Meusel, I., Hartmann, J. & Freund, H. J. A molecular beam/surface spectroscopy apparatus for the study of reactions on complex model catalysts. *Rev. Sci. Instrum.* **71**, 4395–4408 (2000).
23. Parsons, R. The rate of electrolytic hydrogen evolution and the heat of adsorption of hydrogen. *Trans. Faraday Soc.* **54**, 1053–1063 (1958).
24. Zhang, Y. et al. A review on thermalization mechanisms and prospect absorber materials for the hot carrier solar cells. *Sol. Energy Mater. Sol. Cells* **225**, 111073 (2021).
25. Bhattacharya, C. et al. Sustainable nanoplasmon-enhanced photoredox reactions: synthesis, characterization, and applications. *Adv. Energy Mater.* **10**, 2002402 (2020).
26. Xu, Y. & Schoonen, M. A. A. The absolute energy positions of conduction and valence bands of selected semiconducting minerals. *Am. Mineral.* **85**, 543–556 (2000).
27. Janotti, A., Varley, J. B., Choi, M. & Van de Walle, C. G. Vacancies and small polarons in SrTiO₃. *Phys. Rev. B* **90**, 085202 (2014).
28. Chen, H. & Umezawa, N. Hole localization, migration, and the formation of peroxide anion in perovskite SrTiO₃. *Phys. Rev. B* **90**, 035202 (2014).
29. Rubano, A., Paparo, D., Granozio, F. M., Uccio, U. & Marrucci, L. Blue luminescence of SrTiO₃ under intense optical excitation. *J. Appl. Phys.* **106**, 103515 (2009).
30. Mochizuki, S., Fujishiro, F. & Minami, S. Photoluminescence and reversible photo-induced spectral change of SrTiO₃. *J. Phys. Condens. Matter* **17**, 923–948 (2005).
31. Schirmer, O. F. O⁻ bound small polarons in oxide materials. *J. Phys. Condens. Matter* **18**, R667–R704 (2006).
32. Deskins, N. A. & Dupuis, M. Intrinsic hole migration rates in TiO₂ from density functional theory. *J. Phys. Chem. C* **113**, 346–358 (2009).
33. Formal, F. L. et al. Rate law analysis of water oxidation on a hematite surface. *J. Am. Chem. Soc.* **137**, 6629–6637 (2015).
34. Kafizas, A. et al. Water oxidation kinetics of accumulated holes on the surface of a TiO₂ photoanode: a rate law analysis. *ACS Catal.* **7**, 4896–4903 (2017).
35. Waegle, M. M., Chen, X., Herlihy, D. M. & Cuk, T. How surface potential determines the kinetics of the first hole transfer of photocatalytic water oxidation. *J. Am. Chem. Soc.* **136**, 10632–10639 (2014).
36. Mandal, A., Ramasesha, K., Marco, L. D. & Tokmakoff, A. Collective vibrations of water-solvated hydroxide ions investigated with broadband 2DIR spectroscopy. *J. Chem. Phys.* **140**, 204508 (2014).
37. Baiz, C. R., Peng, C. S., Reppert, M. E., Jones, K. C. & Tokmakoff, A. Coherent two-dimensional infrared spectroscopy: quantitative analysis of protein secondary structure in solution. *Analyst* **137**, 1793–1799 (2012).
38. Stewart, G. W. On the early history of the singular value decomposition. *SIAM Rev.* **35**, 551–566 (1993).
39. Guhl, H., Miller, W. & Reuter, K. Water adsorption and dissociation on SrTiO₃ (001) revisited: a density functional theory study. *Phys. Rev. B* **81**, 155455 (2010).
40. Hinojosa, B. B., Van Cleve, T. & Asthagiri, A. A first-principles study of H₂O adsorption and dissociation on the SrTiO₃(100) surface. *Mol. Simul.* **36**, 604–617 (2010).
41. Holmstrom, A., Spijker, P. & Foster, A. S. The interface of SrTiO₃ and H₂O from density functional theory molecular dynamics. *Proc. R. Soc. A* **472**, 20160293 (2016).
42. Roberts, S. T., Ramasesha, K., Petersen, P. B., Mandal, A. & Tokmakoff, A. Proton transfer in concentrated aqueous hydroxide visualized using ultrafast infrared spectroscopy. *J. Phys. Chem. A* **115**, 3957–3972 (2011).
43. Marx, D., Chandra, A. & Tuckerman, M. E. Aqueous basic solutions: hydroxide solvation, structural diffusion, and comparison to the hydrated proton. *Chem. Rev.* **110**, 2174–2216 (2010).
44. Perakis, F., Widmer, S. & Hamm, P. Two-dimensional infrared spectroscopy of isotope-diluted ice Ih. *J. Chem. Phys.* **134**, 204505 (2011).
45. De Marco, L. et al. Differences in the vibrational dynamics of H₂O and D₂O: observation of symmetric and antisymmetric stretching vibrations in heavy water. *J. Phys. Chem. Lett.* **7**, 1769–1774 (2016).
46. Selcuk, S. & Selloni, A. Facet-dependent trapping and dynamics of excess electrons at anatase TiO₂ surfaces and aqueous interfaces. *Nat. Mater.* **15**, 1107–1112 (2016).
47. Swenson, H. & Stadie, N. P. Langmuir’s theory of adsorption: a centennial review. *Langmuir* **35**, 5409–5426 (2019).
48. Cheng, J. & Sprik, M. Acidity of the aqueous rutile TiO₂(110) surface from density functional theory based molecular dynamics. *J. Chem. Theory Comput.* **6**, 880–889 (2010).

Publisher’s note Springer Nature remains neutral with regard to jurisdictional claims in published maps and institutional affiliations.

© The Author(s), under exclusive licence to Springer Nature Limited 2021, corrected publication 2021

Methods

Working electrode and spectro-electrochemical measurements. We obtained 0.08%, 0.5% and 0.7% Nb-doped STO by weight (henceforth 0.08% is referred to as 0.1%) as STO single crystals of size 10 mm × 10 mm × 0.5 mm with crystallographic orientation (100) and polished front sides (surface roughness calculated using an arithmetic average $R_a < 8 \text{ \AA}$) and unpolished backsides from MTI (<https://www.mtixtl.com/srtio3.aspx>). MTI polishes the samples using chemical mechanical polishing, which leads to a range of subsurface defects (threading edge and screw dislocations); assessments of the defect density in SiC used often by the electronics industry give upper limits in the 10^7 cm^{-2} range⁴⁹. For STO, some assessments suggest that mechanical polishing without further annealing or chemical treatment provides “the best compromise in terms of large surface domains, low roughness, absence of oxygen vacancies and absence of atomic structure modification, although with the presence of low level of contaminants at the SrTiO₃ surface”⁵⁰. These carbon contaminants, if present, were removed by electrochemical cycling to achieve smooth cyclic voltammograms in the dark (Supplementary Fig. 1). All spectroscopic measurements were performed on the polished front sides of the as-bought samples. Spectro-electrochemical measurements were performed in a Teflon electrochemical cell with CaF₂ optical windows (3 mm thick). The potential of the n-STO photoelectrode with respect to an Ag/AgCl (3 M KCl) reference electrode (MF-2052; Basi) was controlled by a CHI650E potentiostat (CH Instruments). A Pt wire served as the counter electrode. Ohmic contact between the unpolished n-STO backside and copper wire (working electrode) was established using gallium–indium eutectic (Sigma-Aldrich). For the transient reflectance experiments, an insulating lacquer covered all surfaces except the polished front side of the crystal. The exposed front surface area of the 0.1% and Nb-doped samples accessible by the probe was ~70 mm² on all samples that were used.

Transient reflectance measurements. For the transient experiments, the pump and probe beams were derived from a regeneratively amplified Ti/sapphire laser system (Coherent Legend, Coherent) producing pulses with a centre wavelength of 800 nm and ~150 fs temporal width at a 1 kHz repetition rate. Part of the amplifier output was directed into a third harmonic generation set-up (Eksma FK-800–200-M) to generate 266 nm light as the pump. The pump beam was incident normal to the sample surface. In all experiments, the pump beam was modulated by a mechanical chopper (3501, Newport) at a frequency of 500 Hz. The incident pump fluence was measured to be 0.04 mJ cm⁻², corresponding to carrier densities on the order of 10^{13} cm^{-2} for all sets of transient reflection experiments.

Another part of the 800 nm beam was focused into a 5-mm-thick CaF₂ crystal to generate a white light continuum probe. The CaF₂ crystal was mounted on a stage that rotated the crystal to avoid burning and to generate a stable white light continuum. The portion of the white light continuum that we take into consideration ranges from 365 nm to 730 nm with different intensity for different wavelengths, with 500 nm being the most intense. The leftover fundamental (800 nm) was cut out using an 800 nm notch filter before the probe hits the sample. In order to reduce ghosting artefacts, the broadened portion of the fundamental was cut out with a solution of two dyes (NIR783C and NIR836C), obtained from QCR Solutions, in a cuvette after the probe hit the sample. The incident angle of the probe on the sample was determined to be 35° using the reflection of the sample and the refractive index of water. The polarization of the white light continuum probe beam was controlled and made to be s-polarized with respect to the table by changing the 800 nm polarization using a half-wave plate and a linear polarizer. After the sample, the reflected probe beam was focused into an imaging spectrograph (Isoplane) and charge-coupled device imaging camera (PIXIS) set-up from Princeton Instruments. In addition, <10% of the probe was split before the sample for referencing. Referencing was performed with an unmatched complementary metal–oxide–semiconductor (CMOS) UltraFast Systems spectrometer using the smart referencing algorithm⁵¹ with a 64 compressed pixel array⁵² to achieve a differential probe stability of approximately 2 mOD per pulse pair. The detector outputs were interfaced with a personal computer, which provided automated control over an optical pump–probe delay stage (MTM250CC1; Newport). The probe beam spot size was measured to be 200 μm (full-width at half-maximum, FWHM) horizontally and 50 μm (FWHM) using knife edge measurements.

Laser fluence of 0.04 mJ cm⁻². All spectro-electrochemical measurements were performed with a fluence of 0.04 mJ cm⁻². The fluence was calculated using the pulse energy and the area of the pump beam at the focus. The incident power was measured using a pyroelectric energy sensor (919E-200U-8-25K) from Newport. The pump beam size at the focus was measured by knife edge measurements to be 650 μm × 100 μm (FWHM; Supplementary Fig. 1). The beam was assumed to be spatially Gaussian, and the beam focal area was calculated by assuming an elliptical cross-section.

Sample stage motion. A kinematic mirror mount was attached to the back of the electrochemical cell to allow for proper orientation of the sample surface with respect to the incidence plane of the probe. The whole assembly was mounted on a three-axis stage controlled by programmable actuators (Z 825 B, Thorlabs) and controllers (TDC001, Thorlabs) to move the illuminating spot on the sample continuously during all transient reflection experiments (below), unless otherwise noted. The continuous scanning method was adopted for all transient reflectance experiments to obtain

high-quality data. The continuous movement of the sample allows us to minimize the sample degradation and maintain a stable current of 1.2 mA throughout the experiment (Supplementary Fig. 2). The experiments are carried out by moving the stage such that the illuminating spot raster scans the sample at a controllable speed of $7 \mu\text{m s}^{-1}$, unless stated otherwise. A scan speed of $7 \mu\text{m s}^{-1}$ allows us to do two repeats of the experiment with 2.5 seconds of averaging per delay point (108 delays per repeat) on a single row of the sample (approximately 8 mm of working space per row). One full dataset comprises two experiments done at two different grating positions with four consecutive repeats in each experiment.

Electrolyte solutions. The solutions used were within the range of pH 7–14 with sodium hydroxide (Sigma-Aldrich). The unbuffered solutions were made simply by varying the sodium hydroxide concentration as needed. The buffered solutions were made primarily using sodium monobasic or dibasic phosphate (Sigma-Aldrich) and sodium hydroxide. The pH of the solutions was measured by a calibrated pH meter (catalogue no. 13620631 from Fisher Scientific). In all unbuffered solutions of pH less than or equal to pH 13, the sodium ion concentration was controlled and kept at 100 mM by adding sodium sulfate (Sigma-Aldrich). Ionic strength is represented only by the sodium ion concentration of the solution in question. In all unbuffered solutions of pH less than or equal to pH 13, the sodium ion concentration was controlled and kept at 100 mM by adding sodium sulfate (Sigma-Aldrich). The kinetic isotope effect experiments were carried out twice in unbuffered pH 7 and pH 13 conditions. The first time it was carried out with 200 mM sodium ion concentration using anhydrous sodium sulfate salt. The 100 mM sodium ion concentration was maintained the second time. The pH 7 solution was composed of 99% deuterated water (DLM 7005, Cambridge Isotope Labs) and anhydrous sodium sulfate. The pH 13 solution was composed of sodium deuterioxide (DLM 57-50, Cambridge Isotope Labs) diluted with deuterated water and anhydrous sodium sulfate. The pH of the solutions was measured before and after the experiment, and a correction of 0.456 was applied (for alkaline conditions) to the value obtained from the pH meter.

Data availability

The representative data and all of the analyses from the extended dataset that support the findings of this paper are available in the paper and the Supplementary Information. The extended dataset that supports the findings in this paper is available from the corresponding authors on reasonable request.

References

- Sanchez, E. K. et al. Assessment of polishing-related surface damage in silicon carbide. *J. Electrochem. Soc.* **149**, G131–G136 (2002).
- Arnay, I., Rubio-Zuazo, J. & Castro, G. R. Impact of cleaning methods on the structural properties and morphology of SrTiO₃ surface. *Appl. Surf. Sci.* **427**, 561–565 (2018).
- Feng, Y., Vinogradov, I. & Ge, N.-H. General noise suppression scheme with reference detection in heterodyne nonlinear spectroscopy. *Opt. Express* **25**, 26262–26279 (2017).
- Feng, Y., Vinogradov, I. & Ge, N.-H. Optimized noise reduction scheme for heterodyne spectroscopy using array detectors. *Opt. Express* **27**, 20323–20346 (2019).

Acknowledgements

The experimental work was supported by the Director, Office of Science, Office of Basic Energy Sciences and by the Division of Chemical Sciences, Geosciences and Biosciences of the US Department of Energy at the Renewable and Sustainable Energy Institute (RASEI; Boulder, CO) under contract no. DE-SC0018939 awarded to T.C. This included full support for one postdoctoral fellow and one graduate student, and partial support for another graduate student. We thank C. D. Pemmaraju and H. Frei for helpful discussions.

Author contributions

T.C. conceived of the project, managed the data collection process and wrote the manuscript with the input of all authors. I.V., S.S. and H.L. constructed the transient set-up and collected the transient data. M.P. helped collect the transient data on the highly doped samples. I.V. and A.M. processed the results and analysed the data using principal component analyses. T.C., with input from J.R., developed the theoretical model. J.R. placed the results in the context of previous theoretical models.

Competing interests

The authors declare no competing interests.

Additional information

Supplementary information The online version contains supplementary material available at <https://doi.org/10.1038/s41563-021-01118-9>.

Correspondence and requests for materials should be addressed to Aritra Mandal or Tanja Cuk.

Peer review information *Nature Materials* thanks Bert Weckhuysen and the other, anonymous, reviewer(s) for their contribution to the peer review of this work.

Reprints and permissions information is available at www.nature.com/reprints.